Theoretical Investigation of Molecular Properties of 5-benzyl-6-methyl pyridazine-3-one and 5-benzyl-6-methyl pyridazine-3-thione and their Potentials for Corrosion Inhibition for Steel

Ubong Eduok

College of Engineering, University of Saskatchewan, 57 Campus Drive, Saskatoon, S7N 5A9, Saskatchewan, Canada.
E-mail: ubong.eduok@usask.ca

The present study theoretically investigates the molecular properties of two pyridazine derivatives (5-benzyl-6-methyl pyridazine-3-one, PO and 5-benzyl-6-methyl pyridazine-3-thione, PS) using quantum chemical technique (Parameterization Method 3). It is also an attempt to offer a non-experimental account while justifying the respective contributions of PO and PS molcules as corrosion inhibitors vis-à-vis their adsorption on corroding steel substrates. These molecular level computations were conducted using semi-empirical molecular orbital (MO) technique in *vacuo* and 0 K for spatial molecular structures of pyridazines molecules with full geometry optimization. This was accomplished using the popular Polar-Ribiere algorithm with a convergence set of 0.1 kcal/(Å mol) RMS gradient. Also computed and discussed are the differences in molecular energies (E_{HOMO} and E_{LUMO}), Mulliken interatomic charge, dipole moments, bond lengths and angles, refractivity, polarizability and partition coefficients of both compounds. The obtained theoretical results align with previously reported experimental corrosion behaviours of both compounds. Corrosion inhibition was attributed to the formation of inhibitor layers on steel surface and this further reduced steel corrosion due to electronic activities involving π electron donation via HOMO orbitals of these pyridazines to the empty 3d-orbitals of iron substrate. The compute magnitudes of $E_{binding}$ obtained from molecular dynamic (MD) simulations revealed a strong Fe-surface interaction for PS compared to PO.

1. INTRODUCTION

It has been widely opined that the adsorption of organic inhibitors at metal/solution interfaces reduces anodic dissolution and contributes to corrosion inhibition [1-3]. To a greater extent, apart from other surface phenomena and associated solution factors, the molecular adsorption of these compounds is entirely governed by their chemistries [3]. Molecular properties related to multiple bonds, prevalence

of electron density on donor atoms with π-orbital character, hetero-atoms (O, N, S etc.) and diversity in functional group chemistry, aid metal-surface adsorption. Organic molecules with these heteroatoms possess high electron density clouds that are available for donation while those with multiple bonds also possess π bonds that become adsorption sites [4].
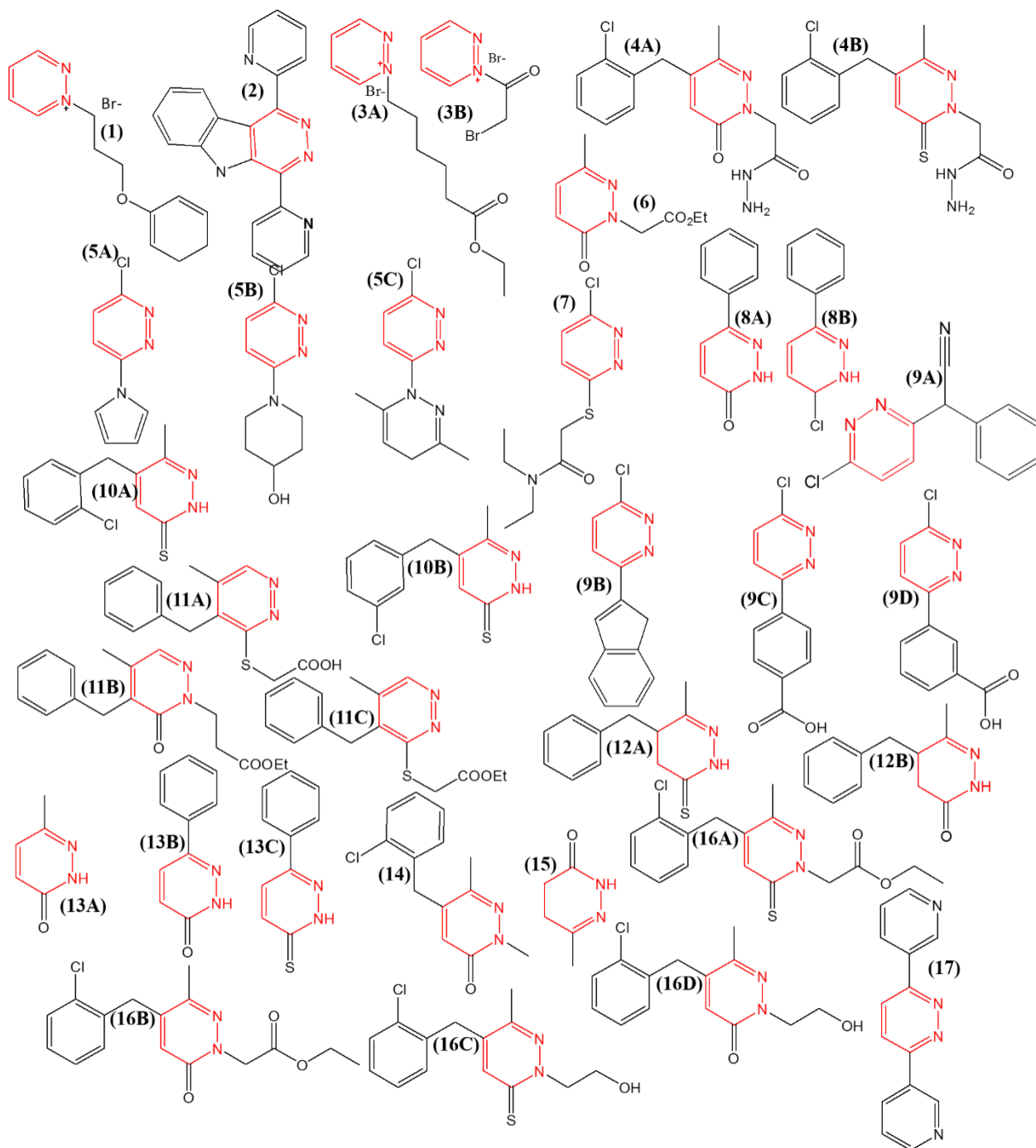

Figure 1. Chemical structures of some pyridazine derivatives utilized as corrosion inhibitors for metal protection in acidic corrosion electrolyte (and their corresponding designated numbers as appeared in each reported system studied in Table 1).

The electronic properties of organic molecules are fundamental in elucidating their surface adsorption activities against aqueous corrosion of metals [4-7]. Other possible atomic/molecular level factors (e.g. electronic structure and approximate molecular weight) and group-binding influences (e.g. presence of phenyl/aromatic groups and electron clouds at donor sites) are also considered when designing corrosion inhibitor composites/systems with promising adsorption and corrosion inhibiting properties [8-10]. Normally, laboratory experiments involving the random testing of available compounds in corrodents for steel (or any other metal substrates) are onerous, expensive and time consuming. Myriads of corrosion inhibitors are reported annually in the literature but the selection criterion for reliable inhibition systems is not governed by traditional testing and experimentation. High frequency computations in modern cheminformatics have proven to be reliable tools for simulating corrosion systems in the presence of inhibitor molecules in a view to understanding their electronic features as they relate to molecular adsorption and corrosion protection.

Modern computational chemistry is an indispensable tool for giving theoretical insights into recent molecular concepts and chemical designs in corrosion science [11-14]. Among existing computation techniques in molecular studies, the application of semi-empirical molecular orbital (MO) method has been widely reported with several models like AM1, CNDO, INDO, MNDO, NDDO, PM3, RM1 and SAM1 [15-18]. Semi-empirical MO method is a quantum computation technique based on the popular Hartree–Fock formalism (HFF). Its approximation is obtained from empirical assertion by excluding the two-electron part of its Hamiltonian. It permits some electron correlation effects mainly due to zero differential overlap approximation. Computation with semi-empirical MO method is quicker compared to some other *ab initio* methods [19]. Semi-empirical MO method is a powerful quantum calculation tool employed in probing the adsorption mechanism of corrosion inhibitor adsorption at metal/solution interfaces. It is also useful in the analyses of reactivity and adsorption behaviours of small molecules in a view to understanding their experimental applications in defined media.

Table 1. Comparative corrosion inhibition performances of different pyridazine derivatives for different metallic substrates in the literature; corrosion inhibition was attributed to the formation of protective inhibitor films on metal surfaces.

S/No.	Pyridazine derivatives	Metallic substrate/Corrodent	*Highest recorded IE (%) at this concentration	Ref.
(1)	1-(3-phenoxypropyl) pyridazin-1-ium bromide**(1)**	Mild steel/1 M HCl	95.29% at 10^{-3}M from weight loss technique	[24]
(2)	1,4-bis(2-pyridyl)-5H-pyridazino[4,5-b]indole**(2)**	Mild steel/1 M HCl	94.0% at 10^{-4} M from weight loss technique	[25]
(3)	1-(6-ethoxy-6-oxohexyl)pyridazin-1-ium bromide **(3A)** and 1-(2-bromoacetyl) pyridazinium bromide **(3B)**	Mild steel/1 M HCl	84% for **3A** and 82% for **3B** at10^{-3} M from EIS technique	[26]
(4)	2-[4-(2-chlorobenzyl)-3-methyl6-oxopyridazin-1(6H)-	Mild steel/0.5 M H_2SO_4	95% at 10^{-4} M from weight loss technique	[27]

	yl]acetohydrazide(**4A**)and 2-[4-(2-chlorobenzyl)-3-methyl-6-thiooxopyridazin-1(6H)-yl]acetohydrazide(**4B**)			
(5)	3-chloro-6-(1H-pyrazol-1-yl)pyridazine(**5A**), 1-(6-chloropyridazin-3-yl)piperidin-4-ol (**5B**), and 3-chloro-6-(3,5-dimethyl-1H-pyrazol-1-yl)pyridazine (**5C**).	Mild steel/1 M HCl	83.04% at 500 ppm from EIS technique	[28]
(6)	Ethyl (6-methyl-3-oxopyridazin-2-yl) acetate(**6A**)	Mild steel/1 M HCl	83.10% at 10^{-3} M from weight loss technique	[29]
(7)	2-((6-chloropyridazin-3-yl)thio)-N,N-diethylacetamide(**7**)	Copper/0.5M H_2SO_4	94.8% at 5 mM from EIS technique	[30]
(8)	6-phenyl-3(2H)-pyridazinone(**8A**) and 3-chloro-6-phenylpyrazine (**8B**)	Mild steel/0.5 M HCl	58.39% and 96.85% at 1.25 mM for **8A** and **8B** from EIS technique	[31]
(9)	2-(6-chloropyridazin-3-yl)-2-phenylacetonitrile (**9A**), 3-(6-chloro-3-pyridazinyl)-1H-indole (**9B**), 4-(6-chloropyridazin-3-yl)benzoic acid (**9C**) and 3-(6-chloropyridazin-3-yl)benzoic acid (**9D**)	Mild steel/1 M HCl	91.35% (**9A**), 92.17% (**9B**), 72.65% (**9C**) and 85.28% (**9D**) at 1 mM from EIS technique	[32]
(10)	5-(2-chlorobenzyl)-6-methylpyridazine-3(2H)-thione(**10A**) and 5-(4-chlorobenzyl)-6-methylpyridazine-3(2H)-thione(**10B**)	Mild steel/0.5 M H_2SO_4	100% and 45% at 5×10^{-4} M **10 B** and **10A**, respectively from weight loss technique	[33]
(11)	5-benzyl-6-methylpyridazin-3-yl thioethanoic(**11A**), (5-benzyl-6-methyl–3-Oxo pyridazin-3-yl) thioethanoic (**11B**) and (5-benzyl-6-methylpyridazin-3-yl) ethyl thioethanoate(**11C**)	Pure iron/1 M HCl	85% (**11A**), 64% (**11B**) and 81% (**11C**) at the 10-4 M from weight loss technique	[34]
**(12)	5-benzyl-6-methyl pyridazine-3-thione (**12A**) and 5-benzyl-6-methyl pyridazine-3-thione (**12B**)	Pure iron/1 M HCl	98% and 80% at 10^{-4} M **12A** and **12B**, respectively,from polarization technique	[35]
(13)	6-methyl-4,5-dihydro-2H-pyridazine3-one (**13A**), 6-phenyl-2H-pyridazine-3-one	Mild steel/1 M HCl	17.7% (**13A**), 25.6% (**13B**), 98.0% (**13C**) at 0.5 mM from weight loss technique	[36]

	(13B) and 6-phenyl-2H-pyridazine-3-thione **(13C)**			
(14)	5-(2-Chlorobenzyl)-2,6-Dimethylpyridazin-3-one	C38 steel/1 M HCl	96.1% at 10^{-3} M from weight loss technique	[37]
(15)	6-methyl-4,5-dihydropyridazin-3(2H)-one	Mild steel/1 M HCl and 0.5 M H_2SO_4	98% in 1 M HCl and 75% in 0.5 M H_2SO_4 at 5.9×10^{-2} M from weight loss technique	[38]
(16)	Ethyl [4-(2-chlorobenzyl)-3-methyl-6-oxopyridazin1(6H)-yl]acetate **(16A)**, ethyl [4-(2-chlorobenzyl)-3-methyl-6-thioxopyridazin-1(6H)-yl]acetate **(16B)**, 5- (2-chlorobenzyl)-2-(2-hydroxyethyl)-6-methylpyridazin-3(2H)-one **(16C)** and 5-(2-chlorobenzyl)-2-(2-hydroxyethyl)-6-methylpyridazine-3(2H)-thione**(16D)**	Mild steel/1 M HCl	100% **(16A)**,92% **(16B)**, 89% **(16C)** and92% **(16D)** at 10^{-3} M from weight loss technique	[39]
(17)	3,6-bis(3-pyridyl)pyridazine **(17)**	Carbon steel/1 M HCl	92.8% at 1.5 mM from weight loss technique	[40]

*Authors in these studies may have utilized of other techniques for studying corrosion monitoring technique, however, the highest recorded values of inhibition efficiency (IE%) were obtained from the mentioned technique.**The current theoretical study is based on this investigation.

Typical examples of corrosion inhibitors are the pyridazine derivatives (5-benzyl-6-methyl pyridazine-3-one (PO) and 5-benzyl-6-methyl pyridazine-3-thione (PS)) previously reported to inhibit the corrosion of pure iron in 1 M HCl [20]. Though the corrosion inhibition performances of other pyridazine derivatives have been reported for pure iron [21] and mild steel [22,23] in 1 M HCl and 0.5 M H_2SO_4 solutions, respectively, the actual inhibition mechanism is not understood. The use of quantum chemical studies in this regard, was totally omitted or in some cases, completely overlooked. The chemical structures of some pyridazine derivatives utilized as corrosion inhibitors in the literature are presented in Figure 1 [24-40]. Their corresponding designated numbers as appeared in each reported system studied in Table 1 are also indicated. Generally, pyridazines are a class of six-membered ring heterocyclic aromatic compounds with two adjacent N atoms (Figure 2). Normal pyridazine is a resonance hybrid of two structures (I and II), though structure I contributes more to the resonance hybrid. Pyridazines were first synthesized from oxidation of benzocinnoline proceeded by rapid decarboxylation of the resulting pyridazinetetracarboxylic acid product. Pyridazines are rare in nature so they are mainly synthesized from hydrazine-catalyzed condensation of ketoacids and/or diketones. Pyridazines are active ingredients in many herbicides and biocides (e.g. pyidate, credazine and pyridafol) as well as medicinal drugs (e.g. pipofezine, cadralazine and cilazapril) [41]. Due to their non-toxic nature, pyridazines utilized in pharmaceutical formulations, as inhibitors of aldose reductase and antioxidants [42].
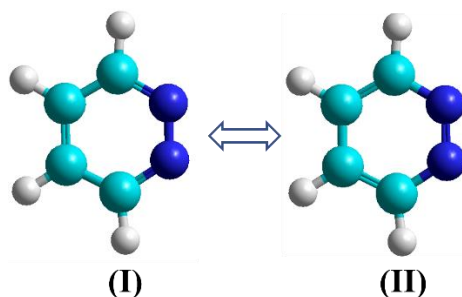
Figure 2. The optimized molecular kekule structures of pyridazine (the two deep blue adjacent atoms are N); Structure I contributes more to the resonance hybrid compared to Structure II.

The corrosion inhibition properties of the aforementioned pyridazine derivatives, PO and PS, have been previously reported experimentally using weight loss, electrochemical polarization and impedance spectroscopy techniques. Corrosion inhibition efficiency was observed to increase with the concentrations of both inhibitor compounds. The highest recorded value of inhibition efficiency against pure iron corrosion was record for PS (98%) compared to PO (80%) [20]. However, this study lacked the insights into the corrosion inhibition mechanism of these pyridazines. To provide a better understanding of the contributions of their structural features on corrosion inhibition, an in-depth theoretical study of molecular and adsorption properties of both pyridazines is proposed for steel. The objective of the present study, therefore, is to ascertain the relationship between some defined quantum chemical parameters and the potency of these molecules toward corrosion inhibition. Relevant quantum chemical parameters (including molecular energy components) and QSAR properties are computed in a view to studying their comparative molecular properties. Molecular plots in the spatial vicinty of optimized PO and PS molecular structures are discussed with respect to their electrostatic charges and total charge densities with full geometry optimization performed using the semi-empirical MO method (PM3 model) with 6-311G^{++} basic sets. There has been no reported theoretical work with indepth molecular explanation of associated corrosion inhbition process with respect to these two compounds in the literature, hence the novelty of the present study. Behzadi et al [43] and Chugh et al [44] have computed similar paramemters for simple pyrazines using DFT. The present work is a theoretical survey offering a strong computational framework in justifying the respective contributions of these compounds to corrosion inhbition. Specific quantum parameters were computed from the magnitudes of orbital energies of stable PO and PS conformers. Molecular dynamics (MD) simulations were also conducted for PO and PS adsorption on Fe surfaces before computing their binding energies.

2. SEMI-EMPIRICAL MO METHODOLOGY

PO and PS are relatively large molecules. In the present study, the semi-empirical MO method is the desired computational tool for theoretically investigating their molecular and adsorption properties. The reasons for this are ascribed to its fast processing time and precision of obtained results; it empirecal approximation is designed to exclude the two-electron integrals normally employed in solving of the partial differential Schrödinger equation (Equation 1) [45].

$$E\Psi = \widehat{H}\Psi \qquad (1)$$

It is widely acceptable that by invoking a normalized condition (Equation 2) to the above equation, the space energy related components in classical mechanics can be rewritten as Equation 3.

$$\int \Psi^2 dV = 1 \qquad (2)$$

$$E = \int \Psi \widehat{H} \Psi dV = \langle \Psi | \widehat{H} | \Psi \rangle \qquad (3)$$

By assuming nuclei stability conditions, knowing that Equation 1 cannot be solved for relatively large molecules (e.g. PO and PS), semi-empirical MO method derived from the HFF assumption can be employed for parameterization [20-46]. Computations with semi-empirical MO method were conducted in this study with a Hyperchem professional 8.0.10 program for Windows, running on a Windows 8.0 OS installed with an Intel Core i7-64 GB RAM-10 TB modeling station. These quantum chemical computations were calculated for parameters that relate the spatial molecular structures and neutral state properties of PO and PS as corrosion inhibitor molecules. Full geometry optimization were also conducted with the parameterization (PM3) approach for these two molecules in *vacuo* and 0 K, using the popular Polar-Ribiere algorithm with a convergence set of 0.001 kcal/(Å mol) RMS gradient with 135 maximum cycles. Molecular dynamics (MD) simulations were carried out for PO and PS adsorption and molecular interactions on a 4×3 supercell, 2.772 Å slab thick Fe (110) surface. MD simulations were performed at chosen boundary conditions for the creation of interfacial model without arbitrary boundary effects in a simulation box (dimension: 9.6084Å × 7.9947Å × 18.9468Å). Prior to MD simulations, the Fe layer with (110) plane was first optimized to minimum energy before placing the PO and PS molecules close to the surface while simulating the molecular interactions with the chosen surface using Materials Studio (version 6.1) program package from Accelrys Inc.

Table 2. Calculated values of gradients, heat of formation and molecular energy components for PO and PS molecules computed with PM3 model.

Molecular properties	PO	PS
RMS gradient (kcal/(Åmol))	0.07412	0.08227
Heat of formation (kcal/mol)	20.98781664	87.55808251
Energies		
Total energy (kcal/mol)	-51281.20090	-48779.46932
Free energy (kcal/mol)	-51281.20090	-48779.46932
E_{LUMO} (eV)	-0.6871572	-1.404247
E_{HOMO} (eV)	-9.167824	-8.671326
ΔE (eV)	8.4806668	7.267079

3. RESULTS AND DISCUSSION

3.1. Geometry optimization and molecular properties

To effectively study the corrosion inhibiting performances of PO and PS, a clear understanding of their spatial molecular and/or electronic structures was necessary in view of explaining their adsorption behaviours on metal substrates [5,47]. This understanding lies in the proper investigation of

the variation in some quantum chemical parameters and in general, the molecular properties of these pyridazines. These quantum parameters play vital roles in the binding characteristics of these compounds at metal/solution interfaces since molecular adsorption proceeds all corrosion inhibition processes [2,48]. The chemical and 3D-optimized structures of PO and PS corrosion inhibitor molecules computed with PM3 method in this study are displayed in Figures (2) and (3).The two molecules are closely related in structure but differ with the O and S substituents at position 9 adjacent to the pyridazinyl group. These atoms are accompanied with lone pairs of electrons that could be donated to empty 3d-orbitals of Fe on the metal substrates (e.g. pure iron) for chemical bonding. The ball-and-stick models used for spatial representations have two hetero-pyridazinyl N atoms at positions 6 and 7, respectively. Both compounds bear benzyl and methyl groups at positions 3 and 4, respectively (Figures 2 and 3(b)) with amu molecular masses of 216.30 and 200.24, for PO and PS, respectively. Prior to any computation, the geometry optimization protocol for each pyridazine was initiated for the chosen PM3 model-based semi-empirical MO technique. Table 2 displays the values of some of the computed quantum chemical parameters. Similar to a related work by Cojocaru et al [45], RMS-gradient values for both molecules were less than the applied 0.1 kcal/(Å mol) convergence. The trend in RMS-gradient values derived confirmed that the semi-empirical model used here optimized the required molecular geometries with minimum energies [20-46].
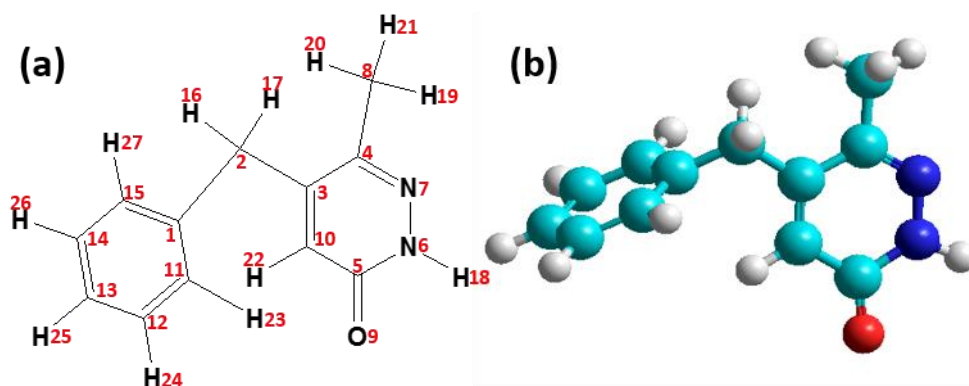

Figure 2. The molecular representations of PO: (a) chemical structure showing labelled atoms; and (b) optimized structure.
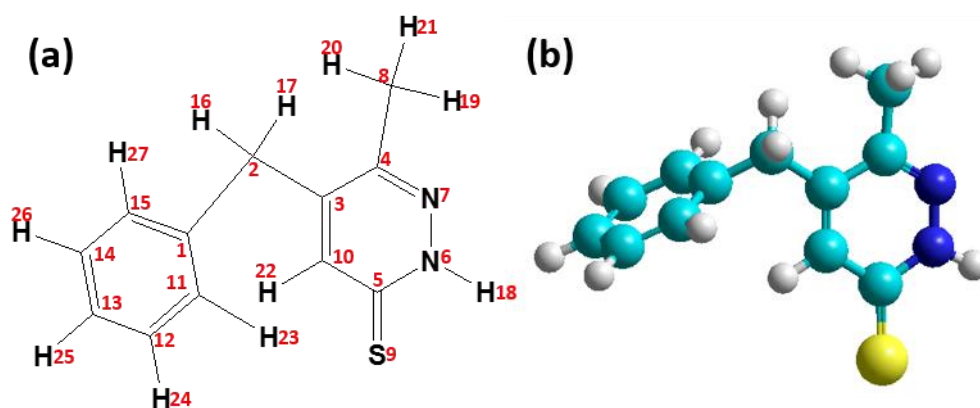

Figure 3. The molecular representations of neutral state PS: (a) chemical structure showing labelled atoms and (b) optimized structure.

Table 3. Variation in values of corrosion inhibition efficiency at 298 K for inhibition of pure iron corrosion in 1 M HCl from three techniques for both compounds.

Inhibitors (10 μM)	Corrosion inhibition efficiency		
	Weight loss	Tafel polarization	EIS technique
PO	74	80	65
PS	98	98	90

Values are obtained from Ref [20]

The computed molecular energies and heat of formation parameters are presented on Table 2. The heat of formation for PO and PS were 20.9 and 87.6 kcal/mol, respectively, while the total energies were predicted at -51281.2 and -48779.5 kcal/mol in that order. As computed by the PM3 model, there are clear differences in the values of the quantum chemical parameter for each inhibitor molecule. These differences could be drawn from the O and S substituents at position 9 of the pyridazinyl group. This trend may go along to suggest that both molecules may have diverse inhibition properties against metal corrosion as revealed by the varying molecular behaviours parameterize with the semi-empirical MO computation.

Semi-empirical MO methods have been known to parameterize accurate geometries and molecular/electronic properties for a wide range of organic compounds and functionalities. Each parameter computed explains the potential inhibition capability of each molecule. Previously reported as inhibitors for pure steel in one molar HCl, PO and PS protected the steel metal substrate up to 80 and 98% corrosion inhibition efficiencies, respectively. PS was regarded as the compound with superior inhibition performance (Table 3). The reason for this could be attributed to the strong adhesion of the PS molecules on iron compared to PO; this was revealed in the superior binding energy of PS over PO (see section 3.5) after MD simulation [48]. Still on binding energy, the actual binding power of the inhibitor molecules (expressed as K_{ads}) to a metal surface is related to ΔG^o_{ads} value by Equation (4); this is another important quantity to evaluate.

$$K_{ads}(mol/L) = -1/55.5 exp[\Delta G^o_{ads}/RT] \qquad (4)$$

Chetouani et al [16] had reported the ΔG^o_{ads} values for PO and PS to be between -47 and -48 kJ/mol, and values within this range are constituent with chemical adsorption on iron surfaces. Molecular chemisorption involves the sharing and/or transfer of electrons between a chemical inhibitor and the metal surface to form coordinate-type bonding [48-50].
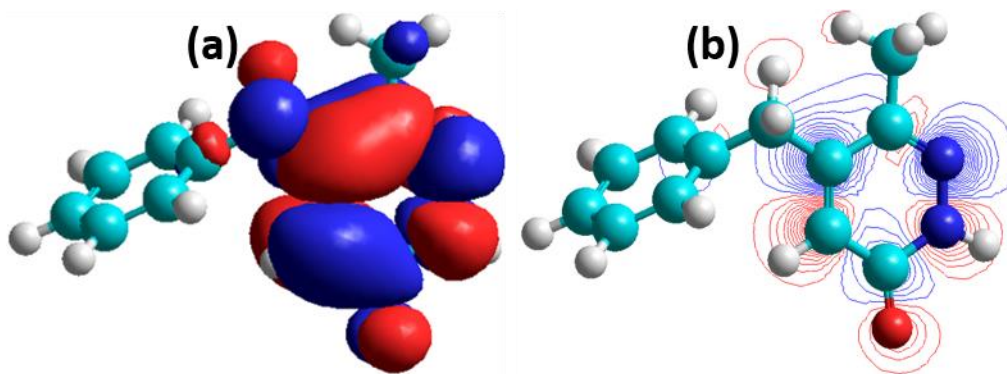
Figure 4. LUMO orbital plots of PO molecule for optimized geometry computed with PM3 method: (a) Gouraud shaded/surfaced 3D isosurface representation and (b) 2D contours.

Figure 5. LUMO orbital plots of PS molecule for optimized geometry computed with PM3 method: (a) Gouraud shaded/surfaced 3D isosurface representation and (b) 2D contours.
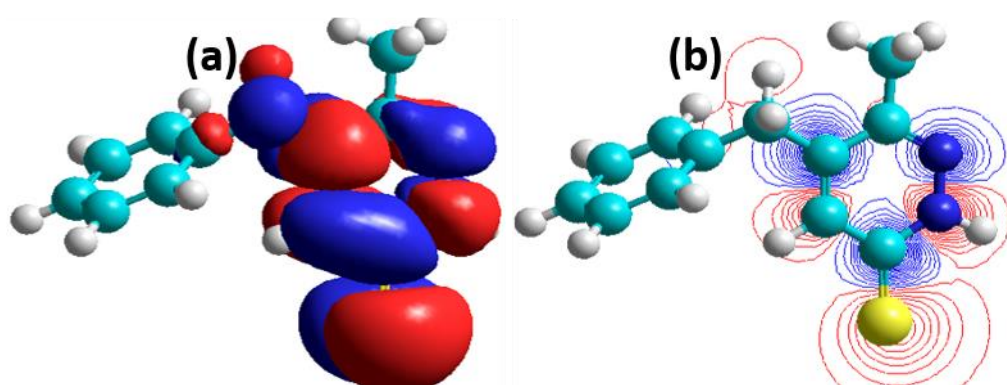
Most likely, the primary cause of the corrosion inhibition effect in the presence of these inhibitor compounds could be consistent with strong adsorption via the pyridazinyl moiety. The lone pairs of electrons on the exocyclic O and S and N heteroatoms may also be readily available for bonding at the metal surface [49]. PS was a better corrosion inhibitor in this study relative to PO. Ideally, molecular absorption at metal surfaces leads to the formation of stable protective adsorptive layer/ thick barriers with increased inhibitor concentrations. This results in reduce metal dissolution rate and limited charge transfer [48,49].

3.2. Energies analyses and related parameters

Semi-empirical MO theoretical computation have proven to be a useful approach in studying the corrosion inhibition potencies of organic compounds in different media [46]. Previous works [43-47] have also shown promising correlations between corrosion inhibition efficiency and molecular energy gap ($\Delta E = E_{LUMO} - E_{HOMO}$) of molecules used as inhibitors. The calculated values of energies for PO and PS were -9.167824 and -8.671326 eV (E_{HOMO}); -0.6871572 and -1.404247 eV (E_{LUMO}), respectively. E_{HOMO} values define the eagerness of these pyridazines to donate electrons for metal surface adsorption,

while E_{LUMO} signifies their unique ability to accept electrons. Substantial increase in E_{HOMO} as well as reduction in ΔE values with inhibitor concentration denotes enhanced corrosion inhibition [43,44]. Relatively small energy gaps are associated with the removal of the last occupied orbital electron during adsorption and bond formations processes; smaller values of ΔE denotes higher corrosion retardation (ΔE_{PO}= 8.4806668 eV and ΔE_{PS} =7.267079). Comparatively for both pyridazine molecules, since $\Delta E_{PS} < \Delta E_{PO}$, this parameter represents another reliable indicator that shows the superior corrosion inhibition performance for PS over PO [20]. Though the difference in ΔE values between both two compounds is not significant, Oguzie et al [51] had opined that strengths of adsorption may be predominantly due to variation in molecular size parameters than electronic properties.

E_{HOMO} and E_{LUMO} for PO and PS were derived from their respective HOMO and LUMO orbital plots for optimized geometry as depicted in Figures (4) to (7). Protonation of these N-heterocyclic inhibitors in acid electrolyte are possible since there is a greater affinity at the pyridazinyl N atom on the cyclic ring. There is also the possibility for coordination bonding between O and S atoms (at position 9) and the empty 3d Fe-orbitals. At the metal surface, molecular adsorption is also dependent on the electron density of these donor atoms. The strengths of adsorption have been reported to increase in the order: S >N >O; hence, the greater corrosion inhibition efficiency of PS compare to PO (Table 3) [49,52,53].

Since molecular kinematics is related to the ability of a molecule to respond to changes in varying conditions of reactions, its stability and chemical reactivity (being a true reflection of ΔE), become a factor in computational quantum chemistry of the molecule [54]. The 2D contours of the HOMO and LUMO orbital plots are accompanied by representative gouraud shaded/surfaced 3D isosurface plots with the blue and red colours representing the positive (+) and negative (-) wave-functions (Ψ_{LUMO} and Ψ_{HOMO}), respectively. Viewing only the pyridazinyl ring from the HOMO plots (Figures 6 and 7), it can be seen that the HOMO levels spread through this moiety for PO than PS. This is more visible on the 2D contour plot with the denser regions representing sites for electrophilic attack (blue contour) [54]. A closer view at these figures reveals that HOMO regions for either molecules (which are reactive centers with the ability to interact with the metal surfaces) are specifically located at C7 and O9, and C3 through C10 for PO, and at C4 and C6 for PS.
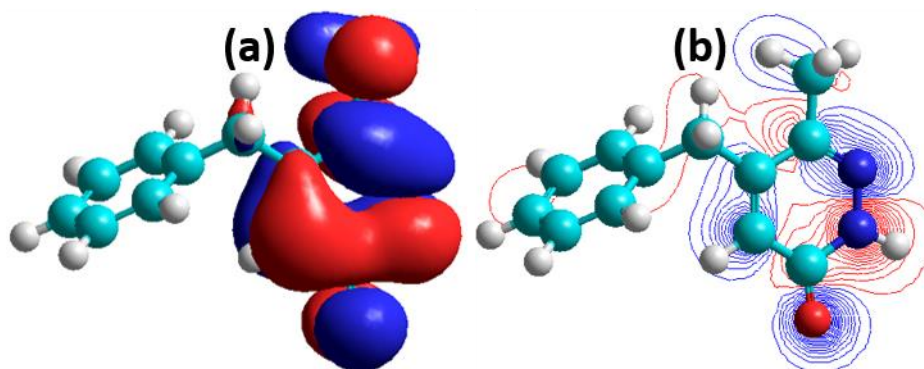

Figure 6. HOMO orbital plots of PO molecule for optimized geometry computed with PM3 method: (a) Gouraud shaded/surfaced 3D isosurface representation and (b) 2D contours.

Figure 7. HOMO orbital plots of PS molecule for optimized geometry computed with PM3 method: (a) Gouraud shaded/surfaced 3D isosurface representation and (b) 2D contours.
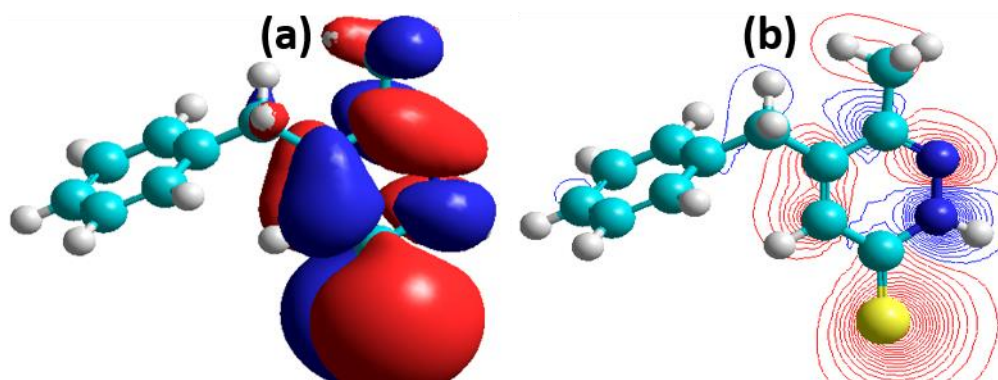
The corresponding Milliken charges at these electron-rich sites are all negative, confirming that the theoretical molecular plots agree with the charge distribution ratio on each pyridazine molecule (except for N6 with a charge magnitude of 0.283 for PS). This discrepancy could have risen from the fact that the actual electronic behaviour of the pyridazinyl ring was strictly determined by the kinetics of electrons in the ring. Also, N6 is nucleophilic, independent for the charge [20,45]. This justifies the availability of the electron pair on N7 in the presence of the electronegative O and S substituents at position 9. It is the presence of these electron donor atoms and the availability of their electrons for bond formations that determine the corrosion efficiencies of inhibitor compounds [48-52]. Unlike HOMO, LUMO regions can accept electrons back-donated from the surfaces of metal surfaces via their anti-bonding orbitals, in turn saturating the pyridazine ring [51].

Quantum structure–activity relations have been widely utilized in correlating metal-surface interactions and molecular structures of organic inhibitor in line with their protective performances by means of semi-empirical methods [54-57]. According to Koopman's theorem explained in the closed-shell Hartree-Fock theory, several quantum descriptors expressed in Equations 5-7 can be derived from frontier orbital energies [58,59].

$$I = -E_{HOMO}; A = -E_{LUMO} \quad (5)$$

In Equation (1), *I* and *A* are designated as ionization potential and electron affinity, respectively. Values of electronegativity (χ), chemical hardness (η), global chemical softness (σ), electrophilicity (ω) and nucleophilicity (ε) for both pyridazines were then computed from Equations 6 and 7. Computed values of these quantum chemical descriptors are presented in Table 4.

$$\chi = \frac{I+A}{2}; \eta = \frac{1-A}{2} \quad (6)$$

$$\sigma = \frac{1}{\eta}; \omega = \frac{\chi^2}{2\eta}; \varepsilon = \frac{1}{\omega} \quad (7)$$

The fraction of electrons transferred (ΔN) from both compounds during the pyridazine/Fe interactions were calculated at magnitudes of η_{Fe} and χ_{Fe} are 0 and 7 eV/mol, respectively [54,58,60].

Table 4. Other quantum chemical descriptors derived from molecular orbital energies

Quantum chemical descriptors (eV)	PO	PS
I	9.167824	8.671326
A	0.687157	1.404247
X	0.843579	1.202124
H	0.156422	-0.202124
$\sigma(eV^{-1})$	6.392987	-4.947470
ω	2.274704	-3.574796
ε	0.439618	-0.279736
ΔN	-19.678961	-14.342410

In the present study, computed values of chemical hardness (η) and global softness (σ) are 0.156 and -0.202 eV; 6.392 and -4.947 eV^{-1}, for PO and PS, respectively. Chemical hardness (η) is the resistance of polarization of electron clouds. It is also referred to as chemical specie deformation [61,62]. Higher values of this parameter for organic inhibitor compounds are consistent with unstable systems; they are unstable for metal-surface adsorption.

Table 5. Mulliken charge distribution for selected atoms of PO and PS molecules.

Mulliken charges	PO	PS
C1	-0.089	-0.096
C2	-0.022	-0.010
C3	-0.023	-0.054
C4	-0.118	-0.062
C5	0.245	-0.144
N6	-0.100	-0.283
N7	-0.093	-0.138
C8	-0.061	-0.070
O9	-0.377	—
S9	—	-0.266
C10	-0.191	-0.111

On the other hand, lower η values of these compounds denote softness, and may mean that these compounds are effective inhibitors due to their highly polarizable electron clouds [63]. The electronegativity (χ) for PO and PS are 0.843 and 1.202 eV. It also represents the ability for these pyridazines to donate electron pairs to form coordinate bonds needed to form protective organic films on metallic surfaces during metal-surface interactions. Effective corrosion inhibitors are strong Lewis bases, and they possess low values of χ. Ionization potential (*I*) is the force field needed to strike off loosely bound electrons while electrophilicity index (ω) denotes the capacity of a molecule to accept electron pairs [63]. In this study and at the PM3 level of approximation, *I* and ω stood at 9.167 and

8.671eV, 2.274 and -3.574 eV, respectively, for PO and PS. For an organic inhibitor compound, nucleophilicity (ε) is the inverse of electrophilicity, and it represents its capacity of share or donate electron pairs (computed values are presented within Table 4). Compounds with low ε or higher ωmagnitudes are consistent with effective protective performance, hence, are effective corrosion inhibitors. The fraction of electrons transferred (ΔN) by PO and PS during pyridazine/Fe interaction were also computed; values of this parameter contribute to the formation of coordination bond during electron transfer [63]. It has been opined that values of ΔN lower than 3.6 denotes electron donating character of inhibitor compounds; inhibition efficiency (IE%) of compounds of this nature increases with their abilities toward electron donation [55,64].

3.3. Charge distribution and QSAR

Most effective corrosion inhibitors are structurally endowed with multiple chemical groups capable of donating electrons to metal surfaces for bond formation as they adsorb on these solid surfaces [24,41]. The magnitude of charges of these chemical groups are also a determining factor toward adsorption; the bigger the magnitude, the eager these groups donate electrons [51]. The computed Mulliken charge distributions of PO and PS for selected atoms are presented on Table 5. These two pyridazines have close charge distribution per atom, with more negative atoms observed at C4 (-0.118), O9 (-0.377) and C10 (-0.191) for PO and C5 (-0.144), C7 (-0.138), S9 (-0.266) and C10 (-0.111) for PS, respectively, indicating most likely adsorption sites. The charges of the benzyl group linking the pyridazine rings via methylene groups at C2 are unchanged for both compounds (not shown on Table 5).

Another molecular parameter that facilitates molecular adsorption, hence corrosion inhibition, is the dipole moment (μ) since it regulates the transport phenomenon of the absorbed layer formed [53,65]. μ values is higher for PS (5.534 D) than PO (3.448 D); this further confirms the reason for superior inhibition ability of PS to PO as reported in Ref [20]. Higher μ denotes higher capacity for molecular adsorption by an inhibitor compound at the metal surface. The negative poles of these compounds lie towards the O and S atoms at position 9 while the positive poles are aligned in the plane of the methylene group at position 2 linking the pyridazine moiety to the phenyl group (not illustrated).
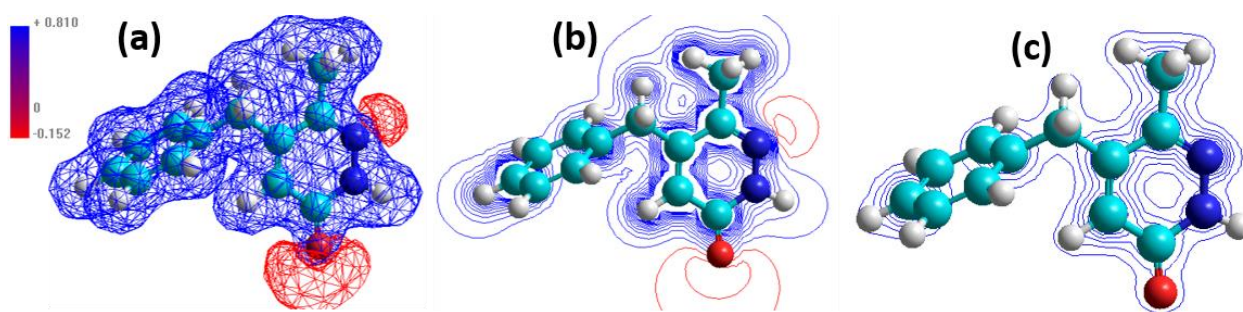

Figure 8. Other molecular plots in the spatial vicinty of optimized PO molecular structure: (a) 3D wired-mesh surfaced umapped isosurface plots. 2D contour maps for electrostatic potential (b) and total charge density (c) of the molecule.

Figure 9. Other molecular plots in the spatial vicinity of optimized PS molecular structure: (a) 3D wired-mesh surfaced umapped isosurface plots. 2D contour maps for electrostatic potential (b) and total charge density (c) of the molecule.
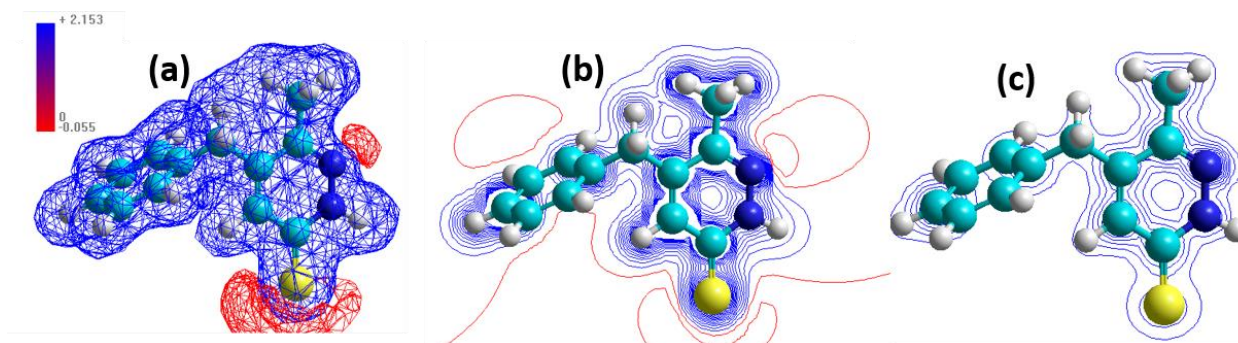
The relationship between charge distribution, dipole moment and electrostatic potential with respected to electrophilic and nucleophilic reactions has been vividly explained by Cojocaru et al [29]. Representing a defined system of charge, electrostatic potential surface (EPS) was modelled in the spatial vicinity of the optimized molecular PO and PS structures. It shows a colour-coded graphics with reliable insight into the molecular properties and association. Figures 8 and 9 depicts molecular plots both wired-mesh surfaced 3D isosurface representations and 2D contour maps for electrostatic potential and total charge density of each pyridazine molecule.The 3D mapped (flat-surfaced; see Figure S1) isosurface plot for PO shows three distinct colored EPS regions; blue, purple and red colours presenting positive, neutral and negative potential regions, respectively.The most negative static-potential regions (deep red) are located around the nucleophilic pyridazinyl N7 and O9 substitient atoms. It has been opined that less negative regions will protonate faster in acid meduim (like 1 M HCl reported in Ref [20]). In this study, N7 is less negative than O9 [45]. These regions are vividly seen on the surfaced 3D unmapped plot (Figure 7a) with bolder wired isosurface markings wound around the atoms at postions 7(N7) and 9 (O9/S9), respectively, for PO and PS molecules. In this same manner, the total valency charge density (TVCD) plots was computed, and the charge density is concentrated at the N7 atomic positions as in the ESP plots, proving that both models are in agreement for the ground state PM3 computation of PO and PS. TVCD distribution is more distinct on the 2D contour maps for both molecules. The charge distributions for both pyridazines differ slightly; this is expected since their molecular structures are the same, only differing with the O and S functionality at position 9 [66]. The QSAR molecular properties computed for PO and PS reasonably varied as displayed on Table 6, though the computed surface areas (both approximated and grid measured in $\mathring{A}^2$) are close. The computed values for refractivity, polarizability and partition coefficient for PO and PS are 71.62 and 63.63 $\mathring{A}^3$, 26.01 and 22.85 $\mathring{A}^3$, and 2.66 and 1.68, respectively.

Table 6. Dipole moment and QSAR properties for PO and PS molecules.

Molecular properties	PO	PS
Dipole moment *(Debyes)*	3.448	5.534
Surface area (approx.) ($Å^2$)	351.12	337.97
Surface area (grid) ($Å^2$)	419.85	400.50
Hydration energy (kcal/mol)	-7.59	-6.10
Log P	2.66	1.68
Refractivity ($Å^3$)	71.62	63.63
Polarizability ($Å^3$)	26.01	22.85
Mass (amu)	216.30	200.24

Table 7. Bond length distribution (Å) for PO and PS molecules.

Bond lengths	PO	PS
C4-C8	1.4906	1.4889
C4=C7	1.3255	1.3303
C4-C3	1.4542	1.4465
N7-N6	1.3433	1.3433
N6-H18	0.9955	0.9960
N6-C5	1.4296	1.4042
C5=O9	1.2244	—
C5=S9	—	1.6310
C5-C10	1.4601	1.4441
C10-H22	1.0984	1.1013
C10=C3	1.3567	1.3636
C3-C2	1.4951	1.4940

Partition coefficient is expressed as the ratio of concentrations of solutes with a solvent. In this study, the range of data is consistent with hydrophobicity [63]. The water-insoluble behaviour of the pyridazines under study can be drawn from the bulky phenyl group attached at position 2. Hydration energy is generally known to be related to ionic-dipole interaction with water; for both pyridazines, the calculated values of this quantity are reasonably close (-7.59 and -6.10 kcal/mol) [63].

3.4. Theoretical bond length and interatomic angles

Theoretical computations were extended to molecular bond lengths (Å) and interatomic angles (°) in order to offer more insights into the frameworks of molecular PO and PS structures. Table 7 shows the bond length distributions for only selected atoms within or close to the pyridazine rings. The calculated bond lengths are ranged between 0.9955 and 1.4951 Å for PO and 0.9960 and 1.6310 Å for PS, respectively. It is proper to point out that the PM3-based computation reproduced similar N-N bond lengths at positions 6 and 7 on the pyridazine ring for both molecules, with only few Å difference for

other selected bond lengths. The difference in the molecular structures of these pyridazines is found in the electronegative atoms at position 9, hence, there is significant change in bond lengths at this position. C-O and C-S bond lengths were computed as 1.2244 and 1.6310 Å, respectively, for PO and PS.

Selected interatomic angles within the pyridazine ring were calculated as presented in Table 8. The shortest angles were ascribed to N7-N6-H18 (114.298°) and C10-C5-N6 (114.288°) for PO and PS, respectively. The widest angles were those of C10-C5-O9 (127.861°) and C5-N6-C7 (124.493°) for PO and PS, in that order. Angles more than or close to 120°, especially C-C-O, C-C-N and C-C-S, are indicative of sp^2 hybridized systems in the pyridazine molecules. The values of the selected torsional angles within and close to the pyridazine rings are negative as presented in Table 8 for two dihedrals per molecule.

Table 8. Selected constraint bond and torsional angles (deg.) for PO and PS molecules

| Bond angles	PO	PS
C10-C3-C4	119.108	118.564
H22-C10-C5	117.956	117.181
C10-C5-O9	127.861	—
C10-C5-S9	—	124.275
O9-C5-N6	116.565	—
S9-C5-N6	—	121.437
C10-C5-N6	115.574	114.288
C5-N6-H18	122.782	120.611
C5-N6-C7	122.918	124.493
N7-N6-H18	114.298	114.896
C2-C3-C4	118.565	118.762
C3-C4-N7	121.038	120.123
C4-N7-N6	120.875	120.697
Torsion angles		
H22-C10-C5-O9	-0.5038	—
H22-C10-C5-S9	—	-0.4537
O9-C5-N6-H18	-0.5932	—
S9-C5-N6-H18	—	-0.3260
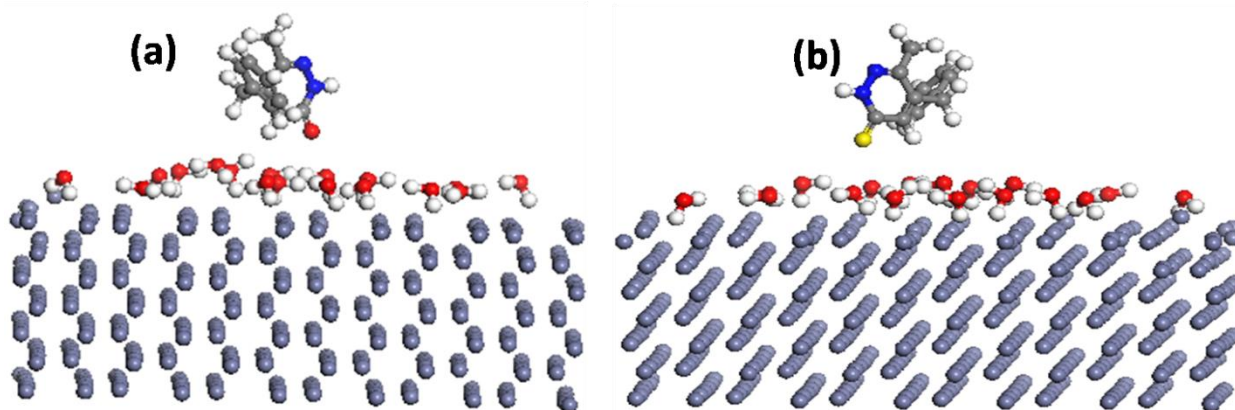
Figure 10. Lateral views of equilibrium PO (a) and PS (b) pyridazine adsorption models on Fe (110) surfaces after molecular dynamics simulation.

However, the calculated bond lengths and interatomic angles presented here are within the level of theory and parameters of PM3 model with a Polar-Ribiere algorithm [66]. There may be discrepancies in the values of these quantities with a few angstroms and degrees, respectively, for bond lengths and angles. Depending on the basic set accompanying any other semi-empirical model utilized for these computations, differences may abound [67,68]. Cojocaru et al [45] previously demonstrated this when comparatively computing the bond angles and lengths of some pyridylindolizine derivatives using MNDO, AM1, RM1 and PM3 models.

3.5. Modeling pyridazine/Fe interactions by MD simulations

In the quest to understand pyridazine/metal interactions surrounding equilibrium adsorption processes, theoretical predictions with MD simulations were carried out in the present study [69]. The energies associated with such interactions as well as their binding strengths to the Fe layers were also computed with a time step and total simulation time of 1 fs and 1 ps, respectively at 1000 steps under 300 K and in NVE ensemble. This followed the same basis set with the LDA/Perdew-Wang correlation. Figure 10 represents the lateral views of equilibrium PO (a) and PS (b) adsorption on Fe (110) surfaces obtained from MD simulation in aqueous media. The pyridazine molecules are presented in parallel orientations on potential binding sites with the exocyclic O and S atoms placed at less than 2 Å distance from the Fe plane. The energy directly linked with the required force associated with pyridazine /Fe surface interaction ($E_{interaction}$) was calculated using Equation 8.

$$E_{binding} = -E_{interaction} \tag{8}$$

The computed magnitudes of $E_{interaction}$ are negative; values up to -84.30 and -94.16 kJ/mol were recorded for PO and PS, respectively. This is indicative of a stable, strong and spontaneous molecular adsorption on the Fe planes by the pyridazines. Normally, more negative values of $E_{interaction}$ obtained between molecules and their adsorbed layers denote high surface binding strength ($E_{binding}$), and this quantity directly describes a molecule's potential toward corrosion inhibition [69,70]. From this study, the computed values of $E_{binding}$ denote strong Fe-surface interaction for PS compared to PO.

This study utilizes an HFF-led quantum computation technique based on a Semi-empirical MO method for geometry optimization. However, in future, comparative structural and orbital energy related information will also be provided using higher DFT basic sets in order to provide more accurate results. Typical examples will include calculations at DFT/B3LYP /6–31 G (d, p), 6-311+G(d,p) and 6-311++G(d,p) levels using Gaussian 09 software program [53,54]. Future studies will also involve the use of several other MO models (e.g. AM1, CNDO, INDO, MNDO, NDDO, PM3, RM1 and SAM1) not only the PM3 method. According to the authors Ref [20], in situ corrosion test was conducted for pure iron aqueous in acid medium. In future, this acidified liquid phase medium will be suitably reflected computationally, in order to account for the acid-solvent effect. The presence of water molecules as well as Cl^- and SO_4^{-2} ions will be included during MD simulations using suitable models (e.g. polarized continuum model (PCM) or conductor-like screening model (COSMO)) [69]. Accompanied adsorption energies for other PO/PS-Fe configurations will also be calculated, relative to the most stable crystal states. This will include Fe (100), Fe (110) and Fe (111) planes at lowest and highest temperatures using

Monte Carlo simulations [69]. Since the experiments were conducted in acid medium, future computations involving quantum chemical descriptors will involve features beyond neutral pyridazines. The adsorption phase properties and inhibitor/Fe interactions on Fe surfaces will be investigated with both neutral and protonated species [70].

4. CONCLUSIONS

This theoretical survery has offered a strong computational framework in justifying, at the molecular level, the individual contributions of two closely related pyridazine compounds to corrosion inhibition. Theoretical computations were based on parameterization (PM3) model of the semi-empirical MO axiom for both molecules. The obtained results from this study for both molecular and adsorption properties suitably predict the strengths of adsorption of both compounds on steel. This study has theoretically evaluated typical molecular bond lengths, interatomic angles and molecular orbital energy spectra. The relationships between charge distribution, dipole moment, electrostatic potential and QSAR molecular properties have been explained with respect to corrosion inhibition. In this study, semi-empirical MO method has proven to be a reliable method for predicting electronic properties and molecular structures, showing promising correlation between the molecular energy gap (E_{LUMO}–E_{HOMO}) and corrosion inhibition efficiency of both pyridazines. The computed energy values for 5-benzyl-6-methyl pyridazine-3-one (PO) and 5-benzyl-6-methyl pyridazine-3-thione (PS) stood at -9.167824 and -8.671326 eV (E_{HOMO}); -0.6871572 and -1.404247 eV (E_{LUMO}), respectively. The computed value of dipole moment for PS was higher (5.534 D) than that of PO (3.448 D). The compute magnitudes of $E_{binding}$ in this study reveal a strong Fe-surface interaction for PS compared to PO. The variation of molecular properties for these pyridazine derivatives from both quantum chemical studies and molecular dynamic simulations confirms the reason PS has superior inhibition ability than PO.

ACRONYMS / ABBREVIATIONS / NOTATIONS

AM1	Austin Method 1
CNDO	Complete Neglect of Differential Overlap
INDO	Intermediate Neglect of Differential Overlap
MNDO	Modified Neglect of Differential Overlap
MO	Molecular orbital
NDDO	Neglect of diatomicDifferential Overlap
PM3	Parameterization Method 3
RM1	Recife Model 1
SAM1	Semi-empirical ab initio Model 1
DFT	Density Function Theory
QSAR	Quantitative structure-activity relationship

LUMO	Lowest unoccupied molecular orbital
HOMO	Highest occupied molecular orbital
HFF	Hartree–Fock formalism
OS	Operating system
GB	Gigabytes
TB	Terabytes
RAM	Read Only Memory
amu	Atomic mass unit

NOTATIONS

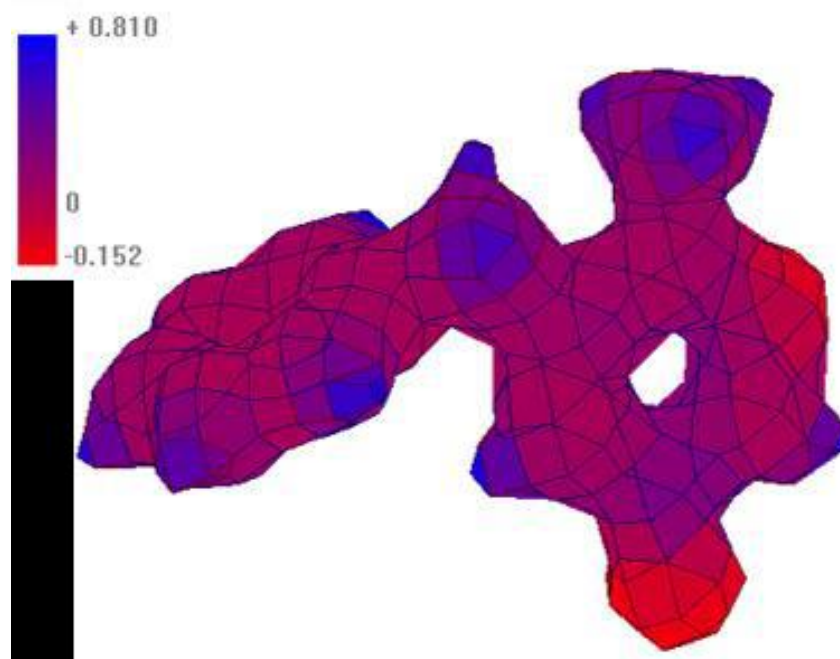| $\widehat{H}$ | Hamiltonian operator: It defines the potentials of electrons as well as their kinetic energies. |
Ψ	Wave-function: it defines the possibility of finding an electron at any specific point in space.
E	Eigenvalue: The eigenvalue of a system defines the energies associated with electron orbitals.
dV	$dxdydz$
x, y, z	Differentials of space coordinates.
μ	Dipole moment

Figure S1. Flat-surfaced 3D mapped isosurface plot of electrostatic potential of optimized PS molecule

References

1.   S.A. Umoren, U.M. Eduok and E.E. Oguzie, *Port. Electrochimica Acta,* 26 (2008) 533.
2.   S.A. Umoren, U.M. Eduok and M.M. Solomon, A.P. Udoh, *Arab. J. Chem.,* 9 (2016) S209.
3.   U.M. Eduok, S.A. Umoren and A.P. Udoh, *Arab. J. Chem.* 5 (2012) 325.
4.   M.A. Bidi, M. Azadia and M. Rassouli, *Mater. Today Commun.,* 24 (2020) 100996.
5.   D.T. Oyekunle, T.I. Oguntade, C.S. Ita, T. Ojo and O.D. Orodu, *Mater. Today Commun.,* 21 (2019) 100691.
6.   I.B. Obot and U.M. Eduok, *J Mol Liq.,* 246 (2017) 66.
7.   X. Yin, H. Wang, S. Sun and E.H. Han, *Mater. Today Commun.,* 24 (2020) 101122.
8.   U. Eduok, O. Faye, E. Ohaeri and J. Szpunar, I. Akpan, *New J Chem.,* 44 (2020) 1117.
9.   U.M. Eduok and M.M. Khaled, *Constr. Build. Mater.* 68 (2014) 285.
10.   U.M. Eduok and M.M. Khaled, *Res. Chem. Intermed.,* 41 (2014) 6309.
11.   A Addoun, S. Bouyegh, M. Dahmane, O. Ferroukhi and M. Trari, *Mater. Today Commun.,* 21 (2019) 100720.
12.   H. Hamani, T. Douadi, M. Al-Noaimi, S. Issaadi, D. Daoud and S. Chafa, *Corros. Sci.,* 88 (2014) 234.
13.   S.N. Rashkeev, M.V. Glazoff and A.Tokuhiro, *J. Nucl. Mater.,* 444 (2014) 56.
14.   S.R. Cross, R.W.S Shademan and C.A. Schuh, *Corros. Sci.,* 77 (2013) 297.
15.   G.B. Rocha, R.O. Freire, A.M. Simas and J.J.P. Stewart, *J. Comput. Chem.,* 27 (2006) 1101.
16.   M.J.S. Dewar and W. Thiel, *J. Am. Chem. Soc.,* 99 (1977) 4907.
17.   R. Karaman, J.L. Huang and J.L. Fry, *J. Comput. Chem.,* 11 (1990) 1009.
18.   J.J.P. Stewart, *J. Comput. Chem.,* 10 (1989) 209.
19.   E.Z. Hückel, *Zur Quantentheorie der Doppelbindung,* 60 (1930) 423.
20.   A. Chetouani, B. Hammouti, A. Aouniti, N. Benchat and T. Benhadd, *Prog. Org. Coat.,* 45 (2002) 373.
21.   A. Chetouani, A. Aouniti, B. Hammouti, N. Benchat, T. Benhadda and S. Kertit, *Corros. Sci.,* 45 (2003) 1675.
22.   M. Bouklah, N. Benchat, B. Hammouti, A. Aouniti and S. Kertit, *Mater. Lett.,* 60 (2006) 1901.
23.   M. Bouklah, N. Benchat, A. Aouniti, B. Hammouti, M. Benkaddour, M.Lagrenee, H.Vezin and F. Bentis, *Prog Org Coat.,* 51 (2004) 118.
24.   F. El-Hajjaji, M. Messali, M.V. Martínez de Yuso, E. Rodríguez-Castellón, S. Almutairi, T.J. Bandosz and M. Algarra, *J. Colloid Interface Sci.,* 541 (2019) 418.
25.   F. Bentiss, F. Gassam, D. Barbry, L. Gengembre, H. Vezin, M. Lagrene and M. Traisnel, *Appl. Surf. Sci.,* 252 (2006) 2684.
26.   F. El-Hajjaji, M. Messali, A. Aljuhani, M.R. Aouad, B. Hammouti, M.E. Belghiti, D.S. Chauhan and M.A. Quraishi, *J. Mol. Liq.,* 249 (2018) 997.
27.   M. Bouklah, N. Benchat, A. Aouniti, B. Hammouti, M. Benkaddour, M. Lagrenee, H. Vezin and F. Bentiss, *Prog. Org. Coat.,* 51 (2004) 118.
28.   L.O. Olasunkanmi, M.E. Mashuga and E.E. Ebenso, Surfaces and Interfaces 12 (2018) 8–19.
29.   A. Ghazoui, N. Benchat, F. El-Hajjaji, M. Taleb, Z. Rais, R. Saddik, A. Elaatiaoui and B. Hammouti, *J. Alloys Compd.,* 693 (2017) 510.
30.   W. Luo, W. Li, J. Tan, J. Liu, B. Tan, X. Zuo, Z. Wang and X. Zhang, *J. Mol. Liq.,* 314 (2020) 11363.
31.   L.O. Olasunkanmi, M.F. Sebona and E.E. Ebenso, *J. Mol. Struct.,* 1149 (2017) 549.
32.   M.E. Mashuga, L.O. Olasunkanmi and E.E. Ebenso, *J. Mol. Struct.,* 1136 (2017) 127.
33.   M. Bouklah, N. Benchat, B. Hammouti, A. Aouniti and S. Kertit, *Mater. Lett.,* 60 (2006) 1901.
34.   A. Chetouani, A. Aouniti, B. Hammouti, N. Benchat, T. Benhadd and S. Kertit, *Corros. Sci.,* 45 (2003) 1675.

35.   A. Chetouani, B. Hammouti, A. Aouniti, N. Benchat and T. Benhadda, *Prog. Org. Coat.,* 45 (2002) 373.
36.   A. Khadiri, R. Saddik, K. Bekkouche, A. Aouniti, B. Hammouti, N. Benchat, M. Bouachrine and R. Solmaz, *J. Taiwan Inst. Chem. E.,* 58 (2016) 552.
37.   H. Zarrok, R. Saddik, H. Oudda, B. Hammouti, A. El Midaoui, A. Zarrouk, N. Benchat and M. EbnTouhami, *Der Pharma Chem.,* 3 (2011) 272.
38.   K. Benbouya, I. Forsal, M. Elbakri, T. Anik, R. Touir, M. Bennajah, D. Chebab, A. Rochdi, B. Mernari and M. EbnTouhami, *Res. Chem. Intermed.,* 40 (2014) 1267.
39.   B. Zerga, R. Saddik, B. Hammouti, M. Taleb, M. Sfaira, M. EbnTouhami, S.S. Al-Deyab and N. Benchat, *Int. J. Electrochem. Sci.,* 7 (2012) 631.
40.   F. Bentiss, M. Outirite, M. Traisnel, H. Vezin, M. Lagrenée, B. Hammouti, S.S. Al-Deyab and C. Jama, *Int. J. Electrochem. Sci.,* 7 (2012) 1699
41.   S. Gumus, *Turkish J. Chem.,* 35 (2011) 803.
42.   P Coudert, E Albuisson, JY Boire, E Duroux, P Bastide and J Couquelet, *Eur. J. Med. Chem.,* 29 (1994) 147.
43.   H. Behzadi, P. Roonasi, M.J. Momeni, S. Manzetti, M.D. Esrafili, I.B. Obot, M. Yousefvand and S.M. Mousavi-Khoshdel, *J. Mol. Struct.,* 1086 (2015) 64.
44.   B. Chugh, AK. Singh, A. Chaouiki, R. Salghi, S. Thakur and B. Pani, *J. Mol. Liq.,* 299 (2020) 112160.
45.   C. Cojocaru, A. Rotaru, V. Harabagiu and L. Sacarescu, *J. Mol. Struct.,* 1034 (2013) 162.
46.   T.G. Gantchev, J.E. van Lier and D.J. Hunting, *Radiat. Phys. Chem.,* 72 (2005) 367.
47.   N.O. Eddy, H.M. Yahaya and E.E. Oguzie, *J. Adv. Res.,* 6 (2015) 6, 203.
48.   S.A. Umoren, M.M. Solomon, U.M. Eduok, I.B. Obot and A.U. Israel, *J. Environ. Chem. Eng.,* 2 (2014) 1048.
49.   S.A. Umoren, I.B. Obot, A.U. Israel, P.O. Asuquo, M.M. Solomon, U.M. Eduok and A.P. Udoh, *J. Ind. Eng. Chem.,* 20 (2013) 3612.
50.   S.A. Umoren, U.M. Eduok, A.U. Israel, I.B. Obot and M.M. Solomon, *Green Chem. Lett. Rev.,* 5 (2011) 303.
51.   E.E. Oguzie, K.L. Oguzie, C.O. Akalezi, I.O. Udeze, J.N. Ogbulie and V.O. Njoku, *ACS Sustain. Chem. Eng.,* 1 (2013) 214.
52.   C.P. Jones, T.B. Scott, J.R. Petherbridge and J. Glascott, *Solid State Ion.,* 231 (2013) 81.
53.   X. Li, S. Deng and X. Xie, *J. Taiwan Inst. Chem. E.,* 45 (2014) 1865.
54.   S. Dahiya, S. Lata, R. Kumar and O.S. Yadav, *J. Mol. Liq.,* 221 (2016) 124.
55.   M.A. Migahed, A.M. Al-Sabagh, E.A. Khamis and E.G. Zaki, *J. Mol. Liq.,* 212 (2015) 360.
56.   M.S. Shihab and H.H. Al-Doori, *J. Mol. Struct.,* 1076 (2014) 658.
57.   G. Bereket, E. Hür and C. Öğretir, *J. Mol. Struc-Theochem.,* 578 (2002) 79.
58.   G. Xia, X. Jiang, L. Zhou, Y. Liao, M. Duan, H. Wang, Q. Pu and J. Zhou, *Corros. Sci.,* 94 (2015) 224.
59.   L.C. Murulana, A.K. Singh, S.K. Shukla, M.M. Kabanda and E.E. Ebenso, *Ind. Eng. Chem. Res.,* 51 (2012) 13282.
60.   Z. El-Adnani, M. Mcharfi, M. Sfaira, M. Benzakour, A.T. Benjelloun and M. Ebn Touhami, *Corros. Sci.,* 68 (2013) 223.
61.   I.B. Obot, S. Kaya, C. Kaya and B. Tüzün, *Physica E,* 80 (2016) 82.
62.   S. Kaya and C. Kaya, *Comput. Theor. Chem.,* 1060 (2015) 66.
63.   U. Eduok, O. Faye and J.Szpunar, *RSC Adv.,* 6 (2016) 108777.
64.   W. Peng, H. Luo and J. Tang, *Corros. Sci.,* 176 (2020) 108918.
65.   R.M. Issa, M.K. Awad and F.M. Atlam, *Appl. Surf. Sci.,* 255 (2008) 2433.
66.   S. Erkoc¸ O.B. Malcioglu and E. Tasci, *J. Mol. Struc-Theochem.,* 674 (2004) 1.
67.   S.S. Rajahram, T.J. Harvey and R.J.K. Wood, *Wear,* 267 (2009) 1883.
68.   Y. Wang, C. Liu, Y. Wang, Q. Li and B. Yan, *Electrochim. Acta,* 331 (2020) 135376.

69.   U.P. Kumar, R.H. Albrakaty, N. Wazzan, I.B. Obot, Z.S. Safi, S. Shanmugan and T. Liang, *Mater Today Commun.,* 22 (2020) 100693
70.   P.K. Paul, M. Yadav and I.B. Obot, *J. Mol. Liq.,* 314 (2020) 113513.